INTERNATIONAL JOURNAL FOR NUMERICAL METHODS IN ENGINEERING
Int. J. Numer. Meth. Engng 2013; **95**:313–330
Published online 24 June 2013 in Wiley Online Library (wileyonlinelibrary.com). DOI: 10.1002/nme.4509

Direct strain tensor approximation for full-field strain measurement methods

Athanasios Iliopoulos[1] and John G. Michopoulos[2,*,†]

[1]*Computational Materials Science Center, George Mason University resident at Naval Research Laboratory, Washington DC, USA*
[2]*Code 6394 Computational Multiphysics Systems Laboratory, Center of Computational Material Science, Naval Research Laboratory, Washington DC, USA*

SUMMARY

Full-field strain measurement techniques are based on computing the spatial derivatives of numerical or functional approximations of the underlying displacement fields extracted from digital imaging methods. These methods implicitly assume that the medium satisfies the strain compatibility conditions, which are only true in the case of a continuum body that remains continuum throughout its deformation history. In the present work, we introduce a method that can be used to calculate the strain components directly from typical digital imaging data, without the need of the continuum hypothesis and the need for displacement field differentiation. Thus, it enables the measurement of strain fields from imaged surfaces that may or may not contain discontinuities. Numerical comparisons are performed on the basis synthetic data produced from an analytical solution for an elastically orthotropic open-hole domain in tension. For performance comparison purposes, the mean absolute error distributions are calculated for the cases of both the traditional meshless random grid method, and the direct strain method introduced herein. It is established that the more refined representation of strain provided by our present approach is more accurate everywhere in the domain, but most importantly, near its boundaries. Published 2013. This article is a US Government work and is in the public domain in the USA.

Received 19 September 2012; Revised 15 January 2013; Accepted 11 March 2013

KEY WORDS: full field; direct strain; digital imaging; MRG; DSI; DIC; meshless; moving least squares

1. INTRODUCTION

Calculation of strain by differentiation of displacement fields is a typical practice in full-field measurement methods [1–15]. In addition, there are techniques, such as Shearography [16–18] and Moiré interferometry [19, 20] that exploit implicit differentiations of the displacement fields, compute only a subset of the strain components, and require specialized instrumentation, are impractical for nonplanar cases and are sensitive to out of plane motions.

Strain field estimation based on differentiation of displacement fields utilized by these techniques implies that the strain compatibility equations remain satisfied for the entire domain of observation over the entire loading history such as the continuum hypothesis remains valid. However, when surface discontinuities or strain localization occur because of damage initiation, the continuum hypothesis is no longer valid throughout the entire field of observation. Therefore, full-field measurement results based on the anticipated validity of the continuous hypothesis yield both inaccurate and indeterminate measurements, thus leading to false qualitative and quantitative conclusions.

Our experience with the utilization of high-throughput multidegree of freedom automated mechatronic testing machines, which are capable of loading specimens multiaxially in conjunction with

*Correspondence to: John G. Michopoulos, Code 6394 Computational Multiphysics Systems Laboratory, Center of Computational Material Science, Naval Research Laboratory, Washington DC 20375, USA.
†E-mail: john.michopoulos@nrl.navy.mil

Report Documentation Page

Form Approved
OMB No. 0704-0188

1. REPORT DATE	2. REPORT TYPE	3. DATES COVERED
24 JUN 2013		**00-00-2013 to 00-00-2013**

4. TITLE AND SUBTITLE	5a. CONTRACT NUMBER
Direct strain tensor approximation for full-field strain measurement methods	5b. GRANT NUMBER
	5c. PROGRAM ELEMENT NUMBER
6. AUTHOR(S)	5d. PROJECT NUMBER
	5e. TASK NUMBER
	5f. WORK UNIT NUMBER
7. PERFORMING ORGANIZATION NAME(S) AND ADDRESS(ES) **Code 6394 Computational Multiphysics System,Laboratory, Center of Computational Material Science,Naval Research Laboratory,Washington,DC,20375**	8. PERFORMING ORGANIZATION REPORT NUMBER
9. SPONSORING/MONITORING AGENCY NAME(S) AND ADDRESS(ES)	10. SPONSOR/MONITOR'S ACRONYM(S)
	11. SPONSOR/MONITOR'S REPORT NUMBER(S)

12. DISTRIBUTION/AVAILABILITY STATEMENT
Approved for public release; distribution unlimited

13. SUPPLEMENTARY NOTES

14. ABSTRACT

15. SUBJECT TERMS

16. SECURITY CLASSIFICATION OF:			17. LIMITATION OF ABSTRACT	18. NUMBER OF PAGES	19a. NAME OF RESPONSIBLE PERSON
a. REPORT **unclassified**	b. ABSTRACT **unclassified**	c. THIS PAGE **unclassified**	**Same as Report (SAR)**	**19**	

energy-based inverse constitutive characterization methodologies for composite materials [21–26], has underlined the need for both automated full-field data processing, but also of an accurate encapsulation of deformation fields. Such concerns become increasingly more important in regions of the specimen that are close to or have undergone failure, and accordingly, the medium can no longer be considered as a continuum. In these areas, the microcracks and cracks developed break the validity of the continuum hypothesis and the associated strain compatibility relations.

Another important issue arising from the derivation of strain from a full-field displacement representation is that of relative lower accuracy near and on the boundaries of the implemented analytical representation [13, 27]. As the strain components are defined in terms of the derivatives of the displacement components, it is expected that the analytical approximation of the strain components will be somewhat problematic, as the displacement approximation does not impose spatially driven constraints on the formulation of its derivatives. Although it is possible to reformulate the meshfree approximation of the displacement fields to take into consideration such information, this would be impractical and would require considerable and customized effort to manually guide the approximation from an algorithmic perspective in a manner that is aware of the boundaries, and it remains general without need for customization from geometry to geometry.

The final issue of concern arises from the fact that if there is noise in the displacement fields, their differentiation will only amplify it for the evaluation of the strain fields.

The challenging character of these issues has driven us to consider a new approach in calculating the full field of strain quantities from full-field digital images of deforming specimens. The numerical and analytical method presented in this paper succeeds in representing the strain tensor field directly from directional engineering strain quantities without requiring or enforcing the satisfaction of the compatibility conditions.

Because this paper aims at introducing direct strain imaging (DSI) as a new full-field measurement method, we first describe the steps involved with the implementation of the traditional meshless random grid (MRG) method [5–15]. This will help delineate the differences and provide the basis of performance comparison between MRG and DSI methods.

The typical experimental procedure for measuring the full field of deformation quantities according to most full field methods in general, and MRG method in particular, can be outlined as follows:

1. A specimen is marked with an appropriate visible pattern that consists of a random distribution of dots distinguishable from the background.
2. If the experiment is to take into consideration out-of-plane motion, two or more cameras are used so that the deformation is stereoscopically reconstructed. The projective characteristics of the cameras are identified through an appropriate calibration procedure [8, 28]
3. The specimen is placed in the mechanical testing machine, and one image per camera is captured in the undeformed configuration prior to the initiation of the loading sequence.
4. While the experiment is taking place, successive images of the deforming specimen are captured.
5. The images are processed and for each frame, the coordinates of appropriate points (nodes) are calculated. Those nodes may be, for example, geometric centroids of dots (for the case of grid methods), appropriate boundaries of geometric entities, correlated subregions (for the case of Digital Image Correlation (DIC)), and so on.
6. Using an interpolation or approximation scheme, a representation of the displacement field is obtained. In the MRG method, the field is represented by a continuous meshless approximation.
7. The strain at any point in the domain is obtained by differentiation of the displacement fields based on the definition of the strain measure as a function of the displacements.

Noise introduced by various sources is the most dominant source of error and plagues all full-field measurement methods. In its presence, the MRG method has been shown to perform very well [13] compared with other methods. The main reason for its improved performance is that the

DOI: 10.1002/nme

approximation scheme of the meshless representation works naturally as a filter that deals exceptionally well with the image acquisition noise. Unfortunately, because not all noise can be removed, there is still room for improving the accuracy levels of full-field techniques for certain experimental configurations.

Following this introduction, the paper continuous with a brief description of the overall problem at hand, and introduces the DSI method by describing a meshless approximation algorithm applied on strain tensor quantities derived from distinct engineering strain component measurements. A proof of the consistency of this approximation follows. The paper continues with presentation of synthetic experiments that are developed to explore the performance of the method on well established full-field representations, based on the deformation of an orthotropic plate with and open hole in tension. The paper closes with conclusions of the current work and future plans.

2. PROBLEM STATEMENT

The engineering strain between pairs of adjacent centroids of dots (nodes) along the directions defined by them, will be the digitally determined data input for the proposed analysis. A domain Ω in the undeformed configuration is shown in Figure 1(a), populated with a number of such nodes. The same domain in the deformed configuration is shown in Figure 1(b). For a set of n nodes in the vicinity of an interest point described by a position vector $\mathbf{w} = \{x_w, y_w\}^{\mathrm{T}}$, it is possible to form a number of engineering strain quantities $e_{ij} = (l'_{ij} - l_{ij})/l_{ij}, i = 1 \ldots n-1, j = 2 \ldots n, i < j$ [29] in terms of the distances l_{ij}, l'_{ij} in the initial and deformed configurations, respectively. Each of those quantities can be considered as the average of the strain component in the direction of the line connecting the two nodes over the respective line segment. Given those engineering strains and the coordinates of the nodes, we seek to calculate the strain tensor at any point $\mathbf{w}$ in the domain. It is important to note that similar to traditional meshless methods [30–32] the vicinity of a point of interest $\mathbf{w} = \{x_w, y_w\}^{\mathrm{T}}$ is bound by an appropriate domain Of support (DOS), and in this work, we will consider the DOS to be circular.

The solution of this problem might be at first considered as the extension of the typical three gauge rosette strain calculation [29]. However, this would only hold true if the strain field is considered constant throughout the region of interest. Indeed, in calculating the strain from a strain rosette, it is assumed that the engineering strains measured by each directional strain gauge of the rosette, all occur at the same point. Although this might be true for certain strain gauge rosette configurations, it is certainly not the case under the requirements of the problem we are attempting to solve because as is evident from Figure 1, the engineering strain quantities cannot be considered as been measured at the same point.

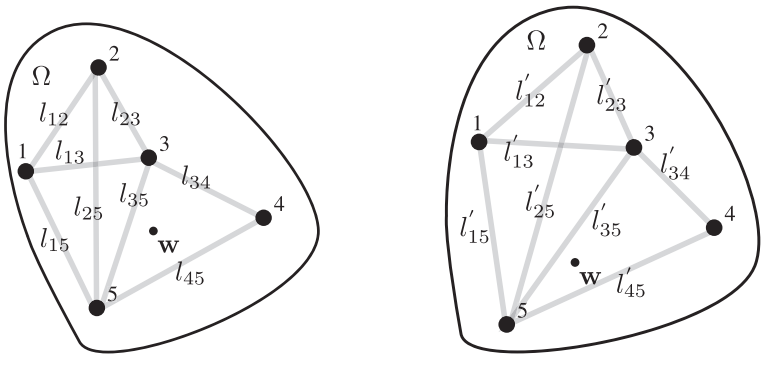

(a) Undeformed (b) Deformed

Figure 1. Deformation configurations and distances of selected node pairs.

DOI: 10.1002/nme

It should be noted that although the method presented herein is used in the context of full-field strain measurements using digital imaging information in the visual spectrum, it can be also applied to any context where appropriate data can be acquired. For example, engineering strain data may be obtained by quantifying separation distances between neighboring markers via the use of ultrasound or X-ray tomography techniques, and the respective full-field strain tensor could be calculated between appropriate volumetric speckles by the method presented in this paper. The same is true for all methods that can identify marker separation on surfaces of deformable bodies.

In the following section, we will present a solution to this problem by the means of a spatial moving least squares approximation.

3. DIRECT STRAIN APPROXIMATION

Our aim is to identify the strain tensor components at any point described by a position vector $\mathbf{w} = \{x_w, y_w\}^{\mathrm{T}}$ within a deformable domain. An approximation of the components of the two-dimensional strain tensor at any point $\mathbf{x} = \{x, y\}^{\mathrm{T}}$ in the vicinity of $\mathbf{w}$ can be expressed by

$$\left.\begin{aligned} \varepsilon^h_{xx}(\mathbf{w};\mathbf{x}) &= \sum_j^m p_j(\mathbf{x}) a_j^{xx}(\mathbf{w}) = \mathbf{p}^{\mathrm{T}}(\mathbf{x})\mathbf{a}^{xx}(\mathbf{w}) \\ \varepsilon^h_{yy}(\mathbf{w};\mathbf{x}) &= \sum_j^m p_j(\mathbf{x}) a_j^{yy}(\mathbf{w}) = \mathbf{p}^{\mathrm{T}}(\mathbf{x})\mathbf{a}^{yy}(\mathbf{w}) \\ \varepsilon^h_{xy}(\mathbf{w};\mathbf{x}) &= \sum_j^m p_j(\mathbf{x}) a_j^{xy}(\mathbf{w}) = \mathbf{p}^{\mathrm{T}}(\mathbf{x})\mathbf{a}^{xy}(\mathbf{w}) \end{aligned}\right\}, \tag{1}$$

where $\mathbf{p}(\mathbf{x})$ is a vector of basis functions that can be chosen to consist of m monomials of the lowest orders to ensure minimum completeness. A polynomial basis of order $M < m$ has the general form

$$\mathbf{p}(\mathbf{x}) = \mathbf{p}(x, y) = \left\{1, x, y, xy, x^2, y^2, \ldots, x^M, y^M\right\}^{\mathrm{T}}. \tag{2}$$

Such a polynomial basis can be constructed by concatenation of the complete order terms using the Pascal triangle of monomials [30, 32]. It should be noted that the polynomial basis could be chosen to be different for each of the strain components, but this would add in algebraic complexity that is not presently justified. In addition, $\mathbf{a}^{\alpha}(\mathbf{w})$ and $\alpha = xx, yy, xy$ are vectors of coefficients specific to every point $\mathbf{w}$ of the domain,

$$\mathbf{a}^{\alpha}(\mathbf{w}) = \{a_0^{\alpha}, a_1^{\alpha}, \ldots, a_m^{\alpha}\}^{\mathrm{T}}, \alpha = xx, yy, xy. \tag{3}$$

In contrast to the MRG method [8], here we are seeking to directly calculate the strain components. Therefore, we first need to identify the engineering strains between a number of node combinations.

The normal strain at an angle θ relative to the global coordinate system is given by the well-known transformation,

$$\varepsilon_{xx'} = \frac{\varepsilon_{xx} + \varepsilon_{yy}}{2} + \frac{\varepsilon_{xx} - \varepsilon_{yy}}{2}\cos 2\theta + \varepsilon_{xy}\sin 2\theta. \tag{4}$$

Using Equations (4) and (1), we can derive the function that approximates the xx strain tensor component at a point $\mathbf{x} = \{x, y\}^T$ on a coordinate system $Ax'y'$ forming an angle θ with the global coordinate system Axy (Figure 2) in the vicinity of $\mathbf{w}$, as follows:

$$\begin{aligned} \varepsilon^h_{xx'}(\mathbf{w};\mathbf{x}) = &\frac{\mathbf{p}^{\mathrm{T}}(\mathbf{x})\mathbf{a}^{xx}(\mathbf{w}) + \mathbf{p}^{\mathrm{T}}(\mathbf{x})\mathbf{a}^{yy}(\mathbf{w})}{2} + \\ &+ \frac{\mathbf{p}^{\mathrm{T}}(\mathbf{x})\mathbf{a}^{xx}(\mathbf{w}) - \mathbf{p}^{\mathrm{T}}(\mathbf{x})\mathbf{a}^{yy}(\mathbf{w})}{2}\cos 2\theta + \\ &+ \mathbf{p}^{\mathrm{T}}(\mathbf{x})\mathbf{a}^{xy}(\mathbf{w})\sin 2\theta, \end{aligned} \tag{5}$$

Published 2013. This article is a US Government work and is in the public domain in the USA.

DOI: 10.1002/nme

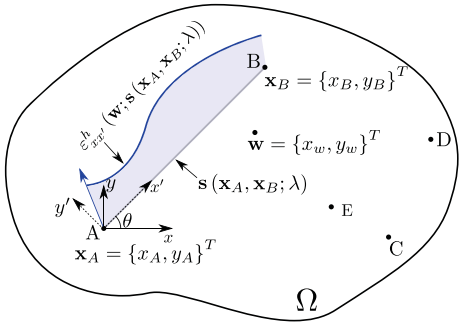

Figure 2. Strain component $\varepsilon^h_{xx'}$ of the approximation in the direction of AB relative to the local coordinate system at point A.

or

$$\begin{aligned}\varepsilon^h_{xx'}(\mathbf{w};\mathbf{x}) = \mathbf{p}^{\mathrm{T}}(\mathbf{x})\mathbf{a}^{xx}(\mathbf{w})\cos^2\theta + \\ + \mathbf{p}^{\mathrm{T}}(\mathbf{x})\mathbf{a}^{yy}(\mathbf{w})\sin^2\theta + \mathbf{p}^{\mathrm{T}}(\mathbf{x})\mathbf{a}^{xy}(\mathbf{w})\sin 2\theta.\end{aligned} \tag{6}$$

Within the domain Ω (Figure 2) and in the vicinity of a point expressed by the vector $\mathbf{w}$, we assume the existence of two neighboring nodes A and B expressed by the vectors $\mathbf{x}_A = \{x_A, y_A\}^{\mathrm{T}}$ and $\mathbf{x}_B = \{x_B, y_B\}^{\mathrm{T}}$, respectively. The mean strain between these two nodes as derived by Equation (6) can be defined by

$$\overline{\varepsilon^h_{xx'}}(\mathbf{w};\mathbf{x}_A,\mathbf{x}_B) = \frac{\int_0^1 \varepsilon^h_{xx'}(\mathbf{w};\mathbf{s}(\mathbf{x}_A,\mathbf{x}_B;\lambda))\left|\frac{\partial \mathbf{s}(\mathbf{x}_A,\mathbf{x}_B;\lambda)}{\partial\lambda}\right|\mathrm{d}\lambda}{|\mathbf{x}_B - \mathbf{x}_A|}, \tag{7}$$

where $\mathbf{s}(\mathbf{x}_A, \mathbf{x}_B; \lambda)$ is the parametric expression of the line segment passing from both A and B and is given by

$$\begin{aligned}\mathbf{s}(\mathbf{x}_A,\mathbf{x}_B;\lambda) = (1-\lambda)\mathbf{x}_A + \lambda\mathbf{x}_B = \\ = \{(1-\lambda)x_A + \lambda x_B, (1-\lambda)y_A + \lambda y_B\}, \lambda \in [0,1].\end{aligned} \tag{8}$$

It is easy to prove that

$$\left|\frac{\partial \mathbf{s}(\mathbf{x}_A,\mathbf{x}_B;\lambda)}{\partial\lambda}\right| = |\mathbf{x}_B - \mathbf{x}_A|, \tag{9}$$

and hence Equation (7) simplifies to

$$\overline{\varepsilon^h_{xx'}}(\mathbf{w};\mathbf{x}_A,\mathbf{x}_B) = \int_0^1 \varepsilon^h_{xx'}(\mathbf{w};\mathbf{s}(\mathbf{x}_A,\mathbf{x}_B;\lambda))\,\mathrm{d}\lambda. \tag{10}$$

The line integral in Equation (10) can then be derived by combining Equations (6) and (8),

$$\begin{aligned}\int_0^1 \varepsilon^h_{xx'}(\mathbf{w};\mathbf{s}(\mathbf{x}_A,\mathbf{x}_B;\lambda))\,\mathrm{d}\lambda = \\ = \int_0^1 \left[\mathbf{p}^{\mathrm{T}}(\mathbf{s})\mathbf{a}^{xx}(\mathbf{w})\cos^2\theta + \right. \\ \left. + \mathbf{p}^{\mathrm{T}}(\mathbf{s})\mathbf{a}^{yy}(\mathbf{w})\sin^2\theta + \mathbf{p}^{\mathrm{T}}(\mathbf{s})\mathbf{a}^{yy}(\mathbf{w})\sin 2\theta\right]\mathrm{d}\lambda.\end{aligned} \tag{11}$$

DOI: 10.1002/nme

The angle θ can be calculated by the nonambiguous arctangent of the vector $\mathbf{x}_B - \mathbf{x}_A$. Splitting up the integral and distributing the independent terms outside the integrands yields

$$\begin{aligned}\int_0^1 \varepsilon^h_{xx'}(\mathbf{w};\mathbf{s}(\mathbf{x}_A,\mathbf{x}_B;\lambda))\,\mathrm{d}\lambda = \\ = \left[\cos^2\theta \int_0^1 \mathbf{p}^{\mathrm{T}}(\mathbf{s}(\mathbf{x}_A,\mathbf{x}_B;\lambda))\,\mathrm{d}\lambda\right]\mathbf{a}^{xx}(\mathbf{w}) + \\ + \left[\sin^2\theta \int_0^1 \mathbf{p}^{\mathrm{T}}(\mathbf{s}(\mathbf{x}_A,\mathbf{x}_B;\lambda))\,\mathrm{d}\lambda\right]\mathbf{a}^{yy}(\mathbf{w}) + \\ + \left[\sin 2\theta \int_0^1 \mathbf{p}^{\mathrm{T}}(\mathbf{s}(\mathbf{x}_A,\mathbf{x}_B;\lambda))\,\mathrm{d}\lambda\right]\mathbf{a}^{xy}(\mathbf{w}).\end{aligned} \tag{12}$$

The vector integrals in Equation (12) can be easily calculated for a given polynomial basis and can be derived from the terms of Table I. If a full-order polynomial is chosen, the integral basis vector can be constructed by concatenation of the respective terms. For example, if a six-term basis vector is chosen to be $\mathbf{p}(\mathbf{x}) = \mathbf{p}(x,y) = \{1,x,y,xy,x^2,y^2\}^{\mathrm{T}}$, the integral basis vector will be

$$\begin{aligned}\mathbf{r}^{\mathrm{T}}(\mathbf{x}_A,\mathbf{x}_B) &= \int_0^1 \mathbf{p}^{\mathrm{T}}(\mathbf{s}(\mathbf{x}_A,\mathbf{x}_B;\lambda))\,\mathrm{d}\lambda \\ &= \left\{1, \frac{1}{2}(x_A+x_B), \frac{1}{2}(y_A+y_B), \frac{1}{6}(x_A(2y_A+y_B)+x_B(y_A+2y_B)),\right. \\ &\quad \left.\frac{1}{3}(x_A^2+x_Ax_B+x_B^2), \frac{1}{3}(y_A^2+y_Ay_B+y_B^2)\right\}.\end{aligned} \tag{13}$$

Table I. Integral basis monomials.

Complete order	Number of terms	Additional terms
Constant	1	1
Linear	3	$\left\{\frac{1}{2}(x_A+x_B), \frac{1}{2}(y_A+y_B)\right\}$
Bilinear	4	$\frac{1}{6}(x_A(2y_A+y_B)+x_B(y_A+2y_B))$
Quadratic	6	$\left\{\frac{1}{3}(x_Ax_B+x_A^2+x_B^2), \frac{1}{3}(y_Ay_B+y_A^2+y_B^2)\right\}$
Quadratic	8	$\left\{\frac{1}{12}(x_A^2(3y_A+y_B)+2x_Ax_B(y_A+y_B)+x_B^2(y_A+3y_B)),\right.$ $\left.\frac{1}{12}(y_A^2(3x_A+x_B)+2y_Ay_B(x_A+x_B)+y_B^2(x_A+3x_B))\right\}$
Cubic	10	$\left\{\frac{1}{4}(x_A+x_B)(x_A^2+x_B^2), \frac{1}{4}(y_A+y_B)(y_A^2+y_B^2)\right\}$
Quartic	15	$\left\{\frac{1}{20}(x_A^3(4y_A+y_B)+x_A^2x_B(3y_A+2y_B)+x_Ax_B^2(2y_A+3y_B)+\right.$ $+x_B^3(y_A+4y_B)),$ $\frac{1}{30}(x_A^2(3y_Ay_B+6y_A^2+y_B^2)+x_Ax_B(4y_Ay_B+3y_A^2+3y_B^2)+$ $+x_B^2(3y_Ay_B+y_A^2+6y_B^2)),$ $\frac{1}{20}(y_A^3(4x_A+x_B)+y_A^2y_B(3x_A+2x_B)+y_Ay_B^2(2x_A+3x_B)+$ $+y_B^3(x_A+4x_B)),$ $\frac{1}{5}(x_A^3x_B+x_A^2x_B^2+x_Ax_B^3+x_A^4+x_B^4),$ $\left.\frac{1}{5}(y_A^3y_B+y_A^2y_B^2+y_Ay_B^3+y_A^4+y_B^4)\right\}$

DOI: 10.1002/nme

The choice of an appropriate polynomial basis will yield an integral vector basis $\mathbf{r}^{\mathrm{T}}(\mathbf{x}_A, \mathbf{x}_B)$. Thus, Equation (12) can be written as

$$\begin{aligned}\int_0^1 \varepsilon^h_{xx'}(\mathbf{w}; \mathbf{s}(\mathbf{x}_A, \mathbf{x}_B; \lambda)) = \\ = \left[\mathbf{r}^{\mathrm{T}}(\mathbf{x}_A, \mathbf{x}_B)\cos^2\theta\right]\mathbf{a}^{xx}(\mathbf{w}) + \\ + \left[\mathbf{r}^{\mathrm{T}}(\mathbf{x}_A, \mathbf{x}_B)\sin^2\theta\right]\mathbf{a}^{yy}(\mathbf{w}) + \\ + \left[\mathbf{r}^{\mathrm{T}}(\mathbf{x}_A, \mathbf{x}_B)\sin 2\theta\right]\mathbf{a}^{xy}(\mathbf{w}),\end{aligned} \tag{14}$$

or

$$\begin{aligned}\int_0^1 \varepsilon^h_{xx'}(\mathbf{w}; \mathbf{s}(\mathbf{x}_A, \mathbf{x}_B; \lambda))\,\mathrm{d}\lambda = \\ = \mathbf{q}^{\mathrm{T}}_{xx}(\mathbf{x}_A, \mathbf{x}_B)\mathbf{a}^{xx}(\mathbf{w}) + \mathbf{q}^{\mathrm{T}}_{yy}(\mathbf{x}_A, \mathbf{x}_B)\mathbf{a}^{yy}(\mathbf{w}) + \\ + \mathbf{q}^{\mathrm{T}}_{xy}(\mathbf{x}_A, \mathbf{x}_B)\mathbf{a}^{xy}(\mathbf{w}),\end{aligned} \tag{15}$$

with

$$\left.\begin{aligned}\mathbf{q}^{\mathrm{T}}_{xx}(\mathbf{x}_A, \mathbf{x}_B) = \mathbf{r}^{\mathrm{T}}(\mathbf{x}_A, \mathbf{x}_B)\cos^2\theta \\ \mathbf{q}^{\mathrm{T}}_{yy}(\mathbf{x}_A, \mathbf{x}_B) = \mathbf{r}^{\mathrm{T}}(\mathbf{x}_A, \mathbf{x}_B)\sin^2\theta \\ \mathbf{q}^{\mathrm{T}}_{xy}(\mathbf{x}_A, \mathbf{x}_B) = \mathbf{r}^{\mathrm{T}}(\mathbf{x}_A, \mathbf{x}_B)\sin 2\theta\end{aligned}\right\}. \tag{16}$$

Collecting the terms of Equation (15) into larger vectors and substituting in (7) yields

$$\overline{\varepsilon^h_{xx'}}(\mathbf{w}; \mathbf{x}_A, \mathbf{x}_B) = \mathbf{q}^{\mathrm{T}}(\mathbf{x}_A, \mathbf{x}_B)\mathbf{a}(\mathbf{w}), \tag{17}$$

with

$$\left.\begin{aligned}&\mathbf{q}^{\mathrm{T}}(\mathbf{x}_A, \mathbf{x}_B) = \left\{q^{AB}_k\right\} = \\ &= \left\{\mathbf{q}^{\mathrm{T}}_{xx}(\mathbf{x}_A, \mathbf{x}_B),\ \mathbf{q}^{\mathrm{T}}_{yy}(\mathbf{x}_A, \mathbf{x}_B),\ \mathbf{q}^{\mathrm{T}}_{xy}(\mathbf{x}_A, \mathbf{x}_B)\right\} \\ &\mathbf{a}(\mathbf{w}) = \{a_k\} = \left\{(\mathbf{a}^{xx}(\mathbf{w}))^{\mathrm{T}}, (\mathbf{a}^{yy}(\mathbf{w}))^{\mathrm{T}}, (\mathbf{a}^{xy}(\mathbf{w}))^{\mathrm{T}}\right\}^{\mathrm{T}} \\ &k = 1 \ldots 3m\end{aligned}\right\}. \tag{18}$$

Equation (17) describes the approximated mean strain between any two nodes in the domain at the vicinity of point $\mathbf{w}$. When the coordinates of the nodes are determined using a digital imaging technique, it is possible to calculate the real mean strain (aka the engineering strain) between any two of the n nodes as

$$e_{ij} = \overline{\varepsilon_{xx'}}(\mathbf{x}_i, \mathbf{x}_j) = \frac{l'_{ij} - l_{ij}}{l_{ij}} = \frac{l'_{ij}}{l_{ij}} - 1 = \frac{|\mathbf{x}'_i - \mathbf{x}'_j|}{|\mathbf{x}_i - \mathbf{x}_j|} - 1, i = 1 \ldots n-1, j = 2 \ldots n, i < j, \tag{19}$$

where $\mathbf{x}_i$ and $\mathbf{x}_j$ are the vectors representing the positions of nodes i, j at the undeformed configuration, and $\mathbf{x}'_i$ and $\mathbf{x}'_j$ are the same vectors in the deformed configuration. The scalar quantities e_{ij} should not be thought of as the elements of a matrix, but rather as a set of $n(n-1)/2$ numbers. Although, not of interest in the current analysis, the latter can be thought as functions of $\mathbf{x}_i$ and $\mathbf{x}_j$ and time. The condition expressing that i should be greater than j ensures the requirement that

DOI: 10.1002/nme

no combination is considered twice. A functional of weighted residuals can now be constructed by using Equations (17) and (19), as follows:

$$\begin{aligned} J &= \sum_{i=1,j=2,i<j}^{n-1,n} W\left(\mathbf{w}-\frac{\mathbf{x}_i+\mathbf{x}_j}{2}\right)\left(\overline{\varepsilon^h_{xx'}}\left(\mathbf{w};\mathbf{x}_i,\mathbf{x}_j\right)-\overline{\varepsilon_{xx'}}(\mathbf{x}_i,\mathbf{x}_j)\right)^2 = \\ &= \sum_{i=1,j=2,i<j}^{n-1,n} W\left(\mathbf{w}-\frac{\mathbf{x}_i+\mathbf{x}_j}{2}\right)\left(\mathbf{q}^T\left(\mathbf{x}_i,\mathbf{x}_j\right)\mathbf{a}(\mathbf{w})-e_{ij}\right)^2, \end{aligned} \tag{20}$$

where $W(\mathbf{w}-(\mathbf{x}_i+\mathbf{x}_j)/2)=W_{ij}\geqslant 0$ is a weight function that decreases with distance as introduced by [30, 32]. A common weight function is the cubic spline weight function given by,

$$W(\mathbf{d})\equiv W(\hat{d})=\begin{cases}\dfrac{2}{3}-4\hat{d}^2+4\hat{d}^3 & ,\hat{d}\leqslant\dfrac{1}{2}\\ \dfrac{4}{3}-4\hat{d}+4\hat{d}^2-\dfrac{4}{3}\hat{d}^3 & ,\dfrac{1}{2}<\hat{d}\leqslant 1\\ 0 & ,\hat{d}>1\end{cases} \tag{21}$$

with $\hat{d}=\frac{|\mathbf{d}|}{d_w}$, the normalized distance, and d_w the smoothing length that is usually equal to the extent of the domain of support.

It should be noted that any strain component could be used in the functional of Equation (20) and that all of them are present in this equation because of Equation (4). The notation $i=1, j=2, i<j$ represents the set of all combinations between the indexes i and j. The least squares minimization of the residual defined by Equation (20) will provide the values of coefficients in the vector $\mathbf{a}(\mathbf{w})$ so that $\overline{\varepsilon^h_{xx'}}(\mathbf{w};\mathbf{x}_i,\mathbf{x}_j)$ optimally approximates $\overline{\varepsilon_{xx'}}(\mathbf{x}_i,\mathbf{x}_j)$. To minimize the residual in Equation (20) with respect to $\mathbf{a}$, we form the derivatives

$$\frac{\partial J}{\partial \mathbf{a}}=\mathbf{0}\implies\frac{\partial J}{\partial a_k}=0, k=1\ldots 3m \tag{22}$$

that can be expanded to

$$\begin{aligned} \frac{\partial J}{\partial a_k} &= \frac{\partial\sum_{i=1,j=2,i<j}^{n-1,n} W_{ij}\left(\sum_{r=1}^{3m} q_r^{ij}a_r-e_{ij}\right)^2}{\partial a_k}= \\ &= 2\sum_{i=1,j=2,i<j}^{n-1,n} W_{ij}\left(\sum_{r=1}^{3m} q_r^{ij}a_r-e_{ij}\right)\frac{\partial\left(\sum_{r=1}^{3m} q_r^{ij}a_r-e_{ij}\right)}{\partial a_k}= \\ &= 2\sum_{i=1,j=2,i<j}^{n-1,n} W_{ij}\left(\sum_{r=1}^{3m} q_r^{ij}a_r-e_{ij}\right)q_k^{ij}= \\ &= 2\sum_{i=1,j=2,i<j}^{n-1,n} W_{ij}\sum_{r=1}^{3m} q_k^{ij}q_r^{ij}a_r-2\sum_{i=1,j=2,i<j}^{n-1,n} W_{ij}q_k^{ij}e_{ij}. \end{aligned} \tag{23}$$

Introducing this expression to Equation (22) yields

$$\sum_{i=1,j=2,i<j}^{n-1,n}\left(W_{ij}\sum_{r=1}^{3m} q_k^{ij}q_r^{ij}a_r\right)=\sum_{i=1,j=2,i<j}^{n-1,n} W_{ij}q_k^{ij}e_{ij}. \tag{24}$$

In matrix notation, the last expression can be written as

$$\mathbf{Q}(\mathbf{w})\mathbf{a}(\mathbf{w})=\mathbf{B}(\mathbf{w})\mathbf{e}_\mathbf{w}, \tag{25}$$

or

$$\mathbf{a}(\mathbf{w})=\mathbf{Q}^{-1}(\mathbf{w})\mathbf{B}(\mathbf{w})\mathbf{e}_\mathbf{w}=\mathbf{M}(\mathbf{w})\mathbf{e}_\mathbf{w}, \tag{26}$$

DOI: 10.1002/nme

where

$$\mathbf{e}_{\mathbf{w}} = \{e_{21}, e_{31}, e_{32}, e_{41}, e_{42}, \ldots, e_{n(n-1)}\}^{\mathrm{T}} \tag{27}$$

is a vector that collects all the measured engineering strains in the vicinity of $\mathbf{w}$, $\mathbf{B}$ is a matrix that has the form

$$\left.\begin{aligned} \mathbf{B}(\mathbf{w}) &= [\mathbf{b}_{21}, \mathbf{b}_{31}, \mathbf{b}_{32}, \mathbf{b}_{41}, \mathbf{b}_{42}, \ldots, \mathbf{b}_{n(n-1)}] \\ \mathbf{b}_{ij}(\mathbf{w}) &= W\left(\mathbf{w} - \frac{\mathbf{x}_i + \mathbf{x}_j}{2}\right)\mathbf{q}(\mathbf{x}_i, \mathbf{x}_j) \end{aligned}\right\}, \tag{28}$$

and $\mathbf{Q}(\mathbf{w})$ is defined by

$$\mathbf{Q}(\mathbf{w}) = \sum_{i=1, j=2, i<j}^{n-1, n} W\left(\mathbf{w} - \frac{\mathbf{x}_i + \mathbf{x}_j}{2}\right)\mathbf{q}(\mathbf{x}_i, \mathbf{x}_j)\mathbf{q}^{\mathrm{T}}(\mathbf{x}_i, \mathbf{x}_j). \tag{29}$$

For the system of Equation (25) to be fully determined the number of equations has to be equal to $3m$, where m is the number of monomials in the polynomial basis. For most cases, the strain values are to be acquired by all the combinations between n nodes, and therefore: $\frac{n(n-1)}{2} = 3m \xrightarrow{m>1} n = \frac{1}{2}\left(1 + \sqrt{1+24m}\right)$. However, an overdetermined system would lead to noise reduction, and thus is preferable. This can be expressed by

$$n \geqslant \frac{1}{2}\left(1 + \sqrt{1+24m}\right). \tag{30}$$

This inequality can be used in conjunction with additional considerations for the identification of the extent of the domain of support and is a topic of a follow-up study.

The matrix $\mathbf{M}(\mathbf{w}) = \mathbf{Q}^{-1}(\mathbf{w})\mathbf{B}(\mathbf{w})$ will be of size $3m \times n$, where each row corresponds to an element of the vectors described in Equation (3).

Partitioning this matrix vertically in three submatrices of dimensions $m \times n$ yields

$$\mathbf{M}(\mathbf{w}) = \begin{bmatrix} \mathbf{M}_{xx}(\mathbf{w}) \\ \mathbf{M}_{yy}(\mathbf{w}) \\ \mathbf{M}_{xy}(\mathbf{w}) \end{bmatrix}. \tag{31}$$

It is now possible to express the coefficients vectors as

$$\left.\begin{aligned} \mathbf{a}^{xx}(\mathbf{w}) &= \mathbf{M}_{xx}(\mathbf{w})\mathbf{e}_{\mathbf{w}} \\ \mathbf{a}^{yy}(\mathbf{w}) &= \mathbf{M}_{yy}(\mathbf{w})\mathbf{e}_{\mathbf{w}} \\ \mathbf{a}^{xy}(\mathbf{w}) &= \mathbf{M}_{xy}(\mathbf{w})\mathbf{e}_{\mathbf{w}} \end{aligned}\right\}. \tag{32}$$

Substitution of these expressions in Equation (1) yields the final form of the fully defined strain field approximation expressions

$$\left.\begin{aligned} \varepsilon^h_{xx}(\mathbf{w}) &\equiv \varepsilon^h_{xx}(\mathbf{w};\mathbf{w}) = \mathbf{\Phi}_{xx}(\mathbf{w})\mathbf{e}_{\mathbf{w}} \\ \varepsilon^h_{yy}(\mathbf{w}) &\equiv \varepsilon^h_{yy}(\mathbf{w};\mathbf{w}) = \mathbf{\Phi}_{yy}(\mathbf{w})\mathbf{e}_{\mathbf{w}} \\ \varepsilon^h_{xy}(\mathbf{w}) &\equiv \varepsilon^h_{xy}(\mathbf{w};\mathbf{w}) = \mathbf{\Phi}_{xy}(\mathbf{w})\mathbf{e}_{\mathbf{w}} \end{aligned}\right\}, \tag{33}$$

where $\mathbf{\Phi}_{\alpha}(\mathbf{w}) = \mathbf{p}^{\mathrm{T}}(\mathbf{w})\mathbf{M}_{\alpha}(\mathbf{w})$, are shape functions of the strain components for the point $\mathbf{w}$ for $\alpha = xx, yy, xy$.

4. CONSISTENCY TEST

A desired but not necessary property of approximations is that of consistency. That is to say, given a field that is expressed by a specific basis function, then it should be reproducible in an exact manner by the approximation when using this basis function.

DOI: 10.1002/nme

Following a similar approach as in [30], we consider that the actual fields of the components of the strain tensor of a domain are given by

$$\left.\begin{aligned}\varepsilon_{xx}(\mathbf{x}) &= \sum_{j}^{k} p_j(\mathbf{x}) c_j^{xx}(\mathbf{x}) \\ \varepsilon_{yy}(\mathbf{x}) &= \sum_{j}^{k} p_j(\mathbf{x}) c_j^{yy}(\mathbf{x}) \\ \varepsilon_{xy}(\mathbf{x}) &= \sum_{j}^{k} p_j(\mathbf{x}) c_j^{xy}(\mathbf{x})\end{aligned}\right\}. \tag{34}$$

We also assume that the same fields are to be approximated by functions of the form given by Equation (1) with $m = k$ and the same basis with Equation (34), that is,

$$\left.\begin{aligned}\varepsilon_{xx}^{h}(\mathbf{x}) &= \sum_{j}^{k} p_j(\mathbf{x}) a_j^{xx}(\mathbf{x}) \\ \varepsilon_{yy}^{h}(\mathbf{x}) &= \sum_{j}^{k} p_j(\mathbf{x}) a_j^{yy}(\mathbf{x}) \\ \varepsilon_{xy}^{h}(\mathbf{x}) &= \sum_{j}^{k} p_j(\mathbf{x}) a_j^{xy}(\mathbf{x})\end{aligned}\right\}. \tag{35}$$

It is obvious that J in Equation (20) will be equal to 0 for $a_j^{\alpha}(\mathbf{w}) = c_j^{\alpha}(\mathbf{x})$ and because J is positive definite, this value will represent the minimum minimorum. In addition, because the sum of Equation (35) yields a linear combination of the coefficients; this minimum will also be unique.

Hence, replacing a_j^{α} with c_j^{α} in (35) yields

$$\varepsilon_{xx}^{h}(\mathbf{x}) = \varepsilon_{xx}(\mathbf{x}), \varepsilon_{xx}^{h}(\mathbf{x}) = \varepsilon_{yy}(\mathbf{x}), \varepsilon_{xx}^{h}(\mathbf{x}) = \varepsilon_{xy}(\mathbf{x}). \tag{36}$$

This proves that the approximated fields of Equation (35) and hence Equation (1) reproduce exactly the fields described by Equation (34).

5. CONDITION NUMBER

As indicated in [33], the effects of the condition number in meshless surface fitting are critical only in the sense of invertibility and do not have a proven relationship with the effectiveness of the regression. Accordingly, in the case of the DSI method, the uniqueness of the solution – as expressed by the condition number – is not of utmost importance either. However, it is worthwhile mentioning that the condition number should not be outrageously high to allow the approximation of the tensor surface from a numerical perspective. To demonstrate this point, we consider the system matrix of interest as indicated in Equation (25) is $\mathbf{Q}$.

To study the effects of the domain of support and the number of monomial terms used in the polynomial basis, a number of numerical tests were performed. A random distribution of nodes was generated in a square domain of a unit length as shown in Figure 3. The matrix $\mathbf{Q}$ was calculated using Equation (29) for a number of domain of support radius values and for a number of monomial terms of the polynomial basis function of Equation (2).

The condition number of matrix $\mathbf{Q}$ is plotted versus the domain of support radius in Figure 4. In this plot, it is observed that for polynomial basis with one and three terms, the condition number is very low, indicating very stable solutions. For higher number of monomial terms, the respective condition numbers tends to be larger but in acceptable ranges especially when compared with other meshless methods [33].

DOI: 10.1002/nme

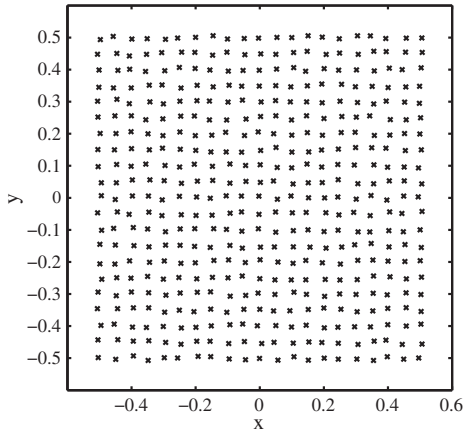

Figure 3. Randomly generated points in a 1×1 domain used in the study of the condition number of $\mathbf{Q}$ of Equation (25).

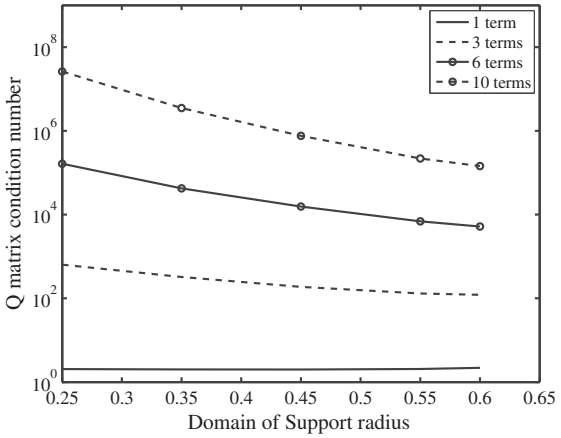

Figure 4. Condition number of matrix $\mathbf{Q}$ versus radius of domain of support for polynomials with various numbers of monomial terms.

6. SYNTHETIC EXPERIMENTS

Because DSI is a consistent approximation, it is expected that it can exactly reproduce simple polynomial fields and hence, it is more interesting to validate it in more realistic and complex situations. To this end, a set of synthetic validation experiments was conducted on a well-known deformation field resulting from the tensile loading of an orthotropic body with a circular hole (Figure 5).

To evaluate the performance of DSI relative to the MRG method, synthetic experiments were developed by applying both methods, and their error relative to the known analytic solution was calculated. The error metric utilized was defined as

$$\left.\begin{aligned} e_m^i &= |\varepsilon_a^i - \varepsilon_m^i| \\ e_d^i &= |\varepsilon_a^i - \varepsilon_d^i| \end{aligned}\right\}, \tag{37}$$

where $i = 1 \ldots N$ is indexing of the N evaluation points, ε_a^i is the strain as calculated from the analytic solution at point i, and ε_m^i and ε_d^i are the strain on point i from the MRG and DSI methods, respectively. The mean absolute error over a set of nodes is calculated by

DOI: 10.1002/nme

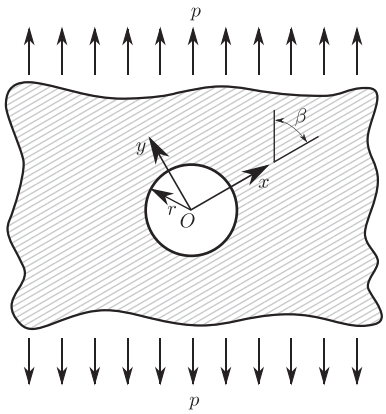

Figure 5. Orthotropic infinite plate with circular hole and load at infinity. Direction of hatch lines coincides with the coordinate system's Ox axis and the major orthotropic direction.

$$\left.\begin{aligned} e_m &= \frac{1}{N}\sum_{i=1}^{N}|\varepsilon_a^i - \varepsilon_m^i| \\ e_d &= \frac{1}{N}\sum_{i=1}^{N}|\varepsilon_a^i - \varepsilon_d^i| \end{aligned}\right\}. \tag{38}$$

Furthermore, because the prevailing source of errors in full-field measurements is that of the noise by the imaging sensor, a simple sensitivity study was conducted for various levels of noise. To investigate the effect, the actual strain field might have on both methods; the synthetic tests with varying load inclination were also conducted.

6.1. Orthotropic plate with open hole

We consider an infinitely large orthotropic elastic plate that contains a circular hole of radius r that is subjected to a stress state at infinity equal to p. The applied load forms an angle β with the major orthotropic axis as shown in Figure 5. This angle essentially controls the degree of anisotropy introduced in the strain–stress fields and varying it amounts to rotating the major orthotropic axis relative to the loading direction (i.e., dual description of the angle). Strain at any point on the plane is expressed by the elastic constitutive equation, [34]

$$\left.\begin{aligned} \varepsilon_{xx} &= a_{11}\sigma_{xx} + a_{12}\sigma_{yy} + a_{16}\tau_{xy} \\ \varepsilon_{yy} &= a_{12}\sigma_{xx} + a_{22}\sigma_{yy} + a_{26}\tau_{xy} \\ \gamma_{xy} &= a_{16}\sigma_{xx} + a_{26}\sigma_{yy} + a_{66}\tau_{xy} \end{aligned}\right\}. \tag{39}$$

It has been shown [34] that the composition of Equation (39) for the general case of multiply connected plane problems can be reduced to a set of algebraic equations in terms of holomorphic functions expressed in the complex plane with the help of the mathematical theory of elasticity. In fact, the general solution to this problem for an elliptic hole is known [35] and is implemented here for an ellipse of minor to major axes aspect ratio of unity, to reflect the problem when the hole is circular. Additional modifications have been introduced [36] to account for rotations of the medium at infinity.

DOI: 10.1002/nme

The stresses are calculated by equation [35]

$$\left.\begin{aligned}\sigma_{xx} &= \sigma_{xx}^{\infty} + 2\mathrm{Re}\left[{s_1}^2\frac{\partial\phi_0(z_1)}{\partial z_1} + {s_2}^2\frac{\partial\psi_0(z_2)}{\partial z_2}\right]\\ \sigma_{yy} &= \sigma_{yy}^{\infty} + 2\mathrm{Re}\left[\frac{\partial\phi_0(z_1)}{\partial z_1} + \frac{\partial\psi_0(z_2)}{\partial z_2}\right]\\ \tau_{xy} &= \tau_{xy}^{\infty} - 2\mathrm{Re}\left[s_1\frac{\partial\phi_0(z_1)}{\partial z_1} + s_2\frac{\partial\psi_0(z_2)}{\partial z_2}\right]\end{aligned}\right\}, \tag{40}$$

where s_1 and s_2 are the roots of

$$a_{11}s^4 - 2a_{16}s^3 + (2a_{12} + a_{66})s^2 - 2a_{26}s + a_{22} = 0. \tag{41}$$

It has been shown [34] that Equation (41) has no real roots and are therefore always of the form

$$s_{1,3} = a_1 \pm b_1 i,\ s_{2,4} = a_2 \pm b_2 i,\ b_1 > 0,\ b_2 > 0. \tag{42}$$

The stress state at infinity is given by

$$\sigma_{xx}^{\infty} = p\cos^2\beta,\ \ \sigma_{yy}^{\infty} = p\sin^2\beta,\ \ \tau_{xy}^{\infty} = p\cos\beta\sin\beta, \tag{43}$$

whereas the holomorphic function is

$$\left.\begin{aligned}\varphi_0(z_1) &= -\frac{ir\left[\sigma_x^{\infty} + is_2\sigma_y^{\infty} + (s_2 + i)\tau_{xy}^{\infty}\right]}{2(s_1 - s_2)}\zeta_1(z_1)\\ \psi_0(z_2) &= -\frac{ir\left[\sigma_x^{\infty} + is_1\sigma_y^{\infty} + (s_1 + i)\tau_{xy}^{\infty}\right]}{2(s_1 - s_2)}\zeta_2(z_2)\end{aligned}\right\}, \tag{44}$$

where

$$\left.\begin{aligned}\zeta_1(z_1) &= \frac{z_1 \pm \sqrt{z_1^2 - r^2(1 + s_1^2)}}{r(1 + is_1)}\\ \zeta_2(z_2) &= \frac{z_2 \pm \sqrt{z_2^2 - r^2(1 + s_2^2)}}{r(1 + is_2)}\end{aligned}\right\}. \tag{45}$$

The sign ambiguity in Equation (45) is removed by requiring $|\zeta_1| \leqslant 1$ and $|\zeta_2| \leqslant 1$. The complex variables are defined in terms of the real position coordinates according to: $z_1 = x + s_1 y$ and $z_2 = x + s_2 y$. Finally, the displacement field components at Ox and Oy directions are given by [36]

$$\left.\begin{aligned}u &= 2\mathrm{Re}[p_1\varphi_0(z_1) + p_2\psi_0(z_2)] + x\varepsilon_{xx}^{\infty} + y\varepsilon_{xy}^{\infty}\\ v &= 2\mathrm{Re}[q_1\varphi_0(z_1) + q_2\psi_0(z_2)] + y\varepsilon_{yy}^{\infty} + x\varepsilon_{xy}^{\infty}\end{aligned}\right\}, \tag{46}$$

with

$$\left.\begin{aligned}p_1 &= a_{11}{s_1}^2 + a_{12} - a_{16}s_1\\ p_2 &= a_{11}{s_2}^2 + a_{12} - a_{16}s_2\\ q_1 &= \frac{a_{12}{s_1}^2 + a_{22} - a_{26}s_1}{s_1}\\ q_2 &= \frac{a_{12}{s_2}^2 + a_{22} - a_{26}s_2}{s_2}\end{aligned}\right\}. \tag{47}$$

DOI: 10.1002/nme

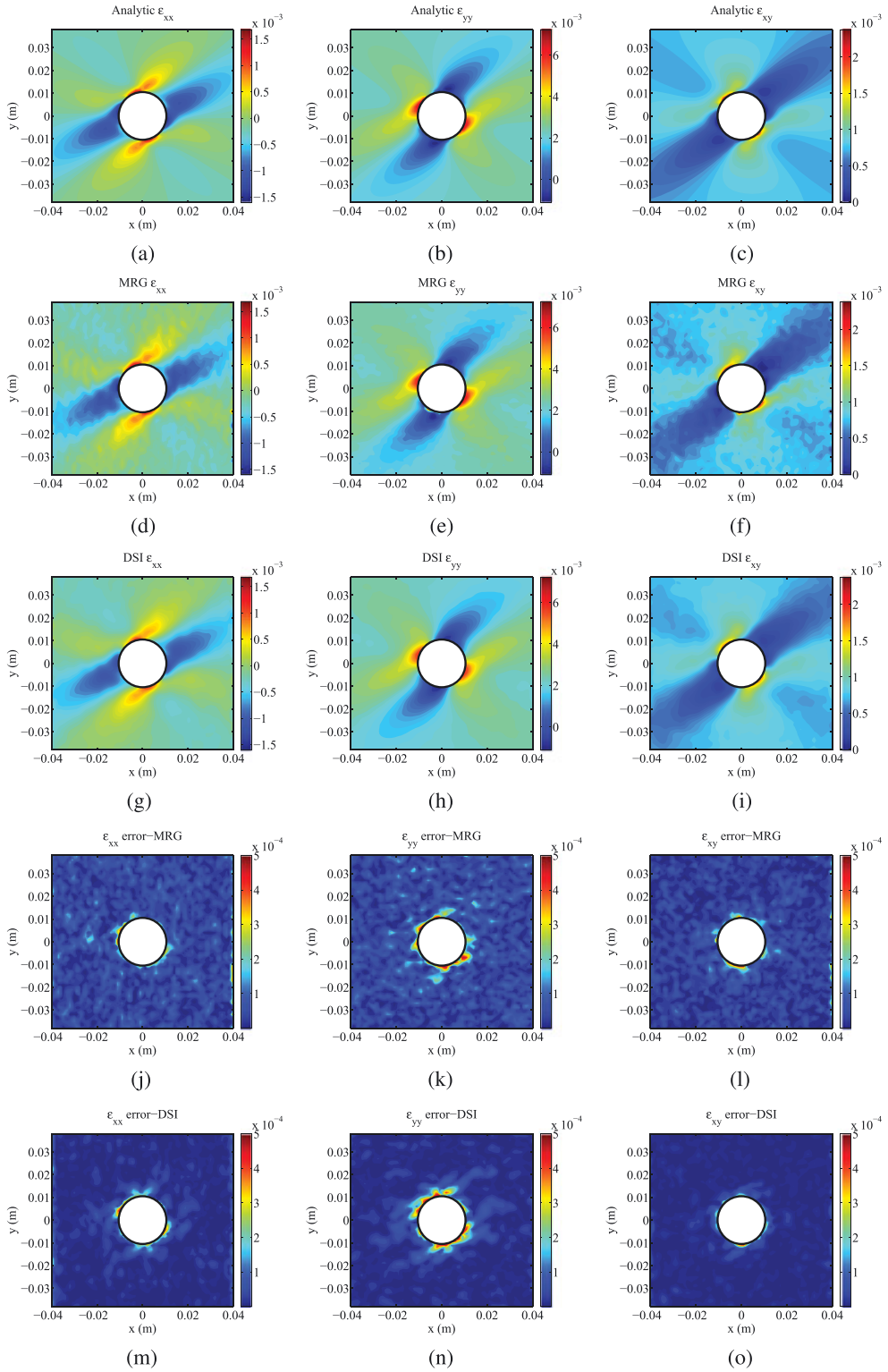

Figure 6. Strain and absolute error contours for nodal noise level of 1×10^{-2} pixels and loading angle of $\beta = 45^{o}$. The domain is assumed to span 1600 pixels wide by 1600 pixels in height. (a)–(c) $\varepsilon_{xx}, \varepsilon_{yy}, \varepsilon_{xy}$ of the analytic solution; (d)–(f) $\varepsilon_{xx}, \varepsilon_{yy}, \varepsilon_{xy}$ of the synthetic experiment using the meshless random grid method; (g)–(i) $\varepsilon_{xx}, \varepsilon_{yy}, \varepsilon_{xy}$ of the synthetic experiment using the DSI method; (j)–(l) respective absolute error of the meshless random grid method; and (m)–(o) respective absolute error of the direct strain imaging method. MRG, meshless random grid; DSI, direct strain imaging.

DOI: 10.1002/nme

6.2. Numerical experiments

To compute the fields for the synthetic numerical experiments, the radius of the hole was selected to be $a = 10^{-2}m$, the stress at infinity $\sigma_\infty = 7 \times 10^5 Pa$, the angle of the major orthotropic axis was $\beta = 45^o$, whereas the extent of the domain of interest (in both the x and y coordinates) was $8a$. The material properties were selected to be

$$\begin{bmatrix} a_{11} & a_{12} & a_{16} \\ a_{12} & a_{22} & a_{26} \\ a_{16} & a_{22} & a_{66} \end{bmatrix} = \begin{bmatrix} 2.245 & -2.732 & 0.000 \\ -2.732 & 9.436 & 0.000 \\ 0.000 & 0.000 & 4.315 \end{bmatrix} \times 10^{-9} Pa^{-1}. \tag{48}$$

A total of 2380 randomly distributed nodes were generated using the method described in [13], whereas the displacement field of Equation (46) was used to generate the displaced nodes, with varying levels of noise. Because for the current digital imaging technology and for most practical applications, the accuracy in coordinate measurement is approximately at the range of 5×10^{-4} to 5×10^{-2} pixels [13]; the noise level was chosen to vary from 10^{-4} to 10^{-1} pixels, assuming the entire domain is mapped on a digital image that is 1600 pixels wide by 1600 pixels high. For the load angle sensitivity trials, the angle β was chosen to vary from 0^o to 90^o, the noise level was kept at 1×10^{-2} pixels, and the synthetic runs were executed 70 times, to also obtain an estimation of the variation of the mean absolute error.

The basis function for MRG was chosen to be of second order (a total of six terms), whereas for the DSI, it was chosen to be of first order (a total of three terms). This choice was made so that the approximation on strains for both methods is of the same polynomial degree. The domain of support radius was chosen at $3.6 \times 10^{-3}m$, whereas the weight function was the one presented in Equation (21).

In Figure 6, the strain contours as well as the absolute error of the MRG and DSI methods are plotted. For those plots, the level of noise imposed on the node coordinates was 1×10^{-2} pixels. It is evident that DSI performs considerably better within the entire domain (Figures 6(m), 6(n), and 6(o)) compared with MRG for all strain components. This fact is more evident in Figure 7, where the mean absolute error of ε_{xx} over the entire domain is plotted for MRG and DSI for various noise levels. The ratio of those errors (bottom graph of Figure 7) reveals that DSI is about at least 1.2 times more accurate than MRG. In the same graph, it can be seen that DSI can be up to 3.3 times more accurate.

Similarly, in Figure 8, the mean absolute error over the boundary of the hole is plotted. In this case as well DSI outperforms MRG by a factor ranging from about 1.2 to about 3.6 times. It is also worthwhile mentioning that DSI performs better with increasing noise levels.

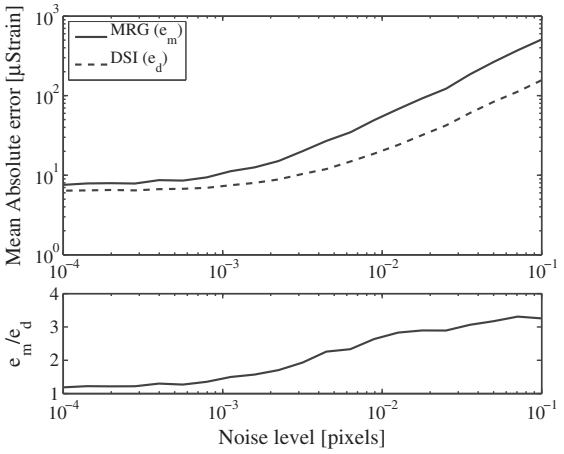

Figure 7. Mean absolute error of ε_{xx} over the interest domain and relative performance of direct strain imaging over meshless random grid (ε_{yy}, ε_{xy} show similar behavior).

Published 2013. This article is a US Government work and is in the public domain in the USA.
Int. J. Numer. Meth. Engng 2013; **95**:313–330
DOI: 10.1002/nme

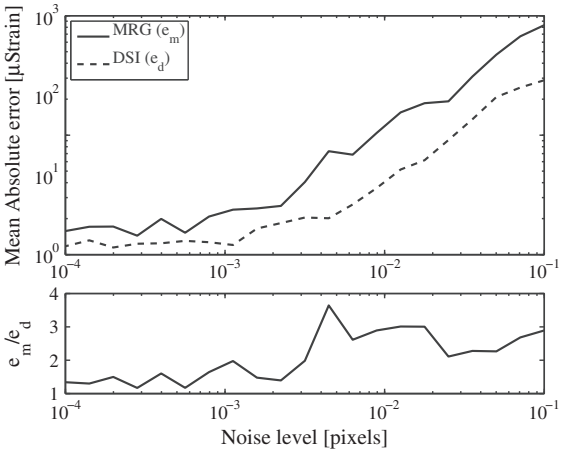

Figure 8. Mean absolute error of ε_{xx} over the hole boundary and relative performance of direct strain imaging over meshless random grid (ε_{yy}, ε_{xy} show similar behavior).

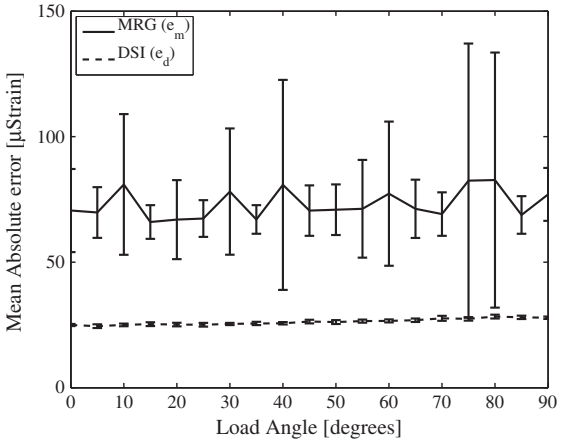

Figure 9. Mean absolute error of ε_{xx} over the entire domain versus load angle (ε_{yy} and ε_{xy} show similar behavior). For each load angle, 70 trials were performed, and their standard deviation is shown as the error bars in the graph. It is worthwhile noting that the standard deviation of the direct strain imaging error is very small and the error bars are almost indistinguishable from the trend line.

Both methods seem to reach a plateau for noise levels below 2×10^{-3}, which is anticipated to depend on the spatial density of the nodes. It should be noted that for most practical cases the displacement noise levels are between 5×10^{-3} to 10×10^{-3} that give the DSI an average performance markup of about 3 times for both error metrics.

Finally, in Figure 9, the mean absolute error of each of the methods is plotted with respect to the loading angle as this induces the strain variability due to the specific nature of the anisotropic elastic problem at hand. As expected, the average of the mean error is not affected by the load angle, but for the MRG method, its deviation (i.e., the error of the error) is considerably larger. This observation further supports the utilization of the DSI method in applications where the knowledge of the uncertainty of the full-field measurements is of importance.

7. CONCLUSIONS

In this work, the numerical foundation of the DSI method was presented and its accuracy relative to the MRG method was assessed. DSI outperformed MRG both on the regions near the domain boundaries, where full field methods traditionally suffer, but also on the rest of the domain of interest. For the chosen medium configuration, DSI was found to be at least 1.2 times more accurate,

DOI: 10.1002/nme

while there were tests where it achieved an accuracy improvement of up to 3.6 times. It was established that at the noise levels of the most popular digital imaging devices, DSI outperforms MRG by a factor of 3 in terms of the mean absolute error. DSI also proved to be very robust and numerically stable in terms of mean error deviation, as was shown by repeated numerical experiments under the same image sensor noise levels.

Furthermore, DSI does not make any explicit or implicit assumptions on the continuity of the underlying field, and therefore, it can be used on media that either cannot be considered continua or have developed cracks or otherwise failed.

In a more general setting, the analysis presented herein introduces a method for approximating tensor quantities with respect to its transformation law, from directional component measurements, rather than a scalar quantity that is usually the case for typical regression analysis approaches.

Future plans include the development of a more detailed analysis for DSI with respect to the parameters that affect its performance (noise level, node density, choice of polynomial basis, and choice of DOS), as well as comparison of its performance and validation with actual experimental data obtained by strain gauge measurements.

ACKNOWLEDGEMENTS

The authors acknowledge the support of the Office of Naval Research under contract N0001412WX21199 and the 6.1 core funding by the Naval Research Laboratory.

REFERENCES

1. Sevenhuijsen J. Two simple methods for deformation demonstration and measurement. *Strain* 1981; **17**(1):20–24. http://onlinelibrary.wiley.com/doi/10.1111/j.1475-1305.1981.tb00357.x/references.
2. Andersen K, Helsch R. Calculation of grating coordinates using correlation filter techniques. *Optik* 1988; **80**:76–79.
3. Bruck H, McNeill S, Sutton M, Peters W. Digital image correlation using Newton-Raphson method of partial differential correction. *Experimental Mechanics* 1989; **29**:261–267. DOI: 10.1007/BF02321405. http://dx.doi.org/10.1007/BF02321405.
4. Sirkis J, Lim T. Displacement and strain measurement with automated grid methods. *Experimental Mechanics* 1991; **31**:382–388. DOI: 10.1007/BF02325997. http://dx.doi.org/10.1007/BF02325997.
5. Andrianopoulos NP, Iliopoulos AP. *Strain Measurements by a Hybrid Experimental-Numerical Method using a Mesh-free Field Function, Honorary Volume for Professor P. S. Theocaris*. Armenian Academy of Sciences: Yerevan, 2005, 31–41.
6. Andrianopoulos NP. Full-Field displacement measurement of a speckle grid by using a Mesh-Free deformation function. *Strain* 2006; **42**(4):265–271. DOI: 10.1111/j.1475-1305.2006.00287.x. http://onlinelibrary.wiley.com/doi/10.1111/j.1475-1305.2006.00287.x/abstract.
7. Andrianopoulos NP, Iliopoulos AP. Displacements measurement in irregularly bounded plates using mesh free methods. *Proceedings of the 16th European Conference of Fracture*, Alexandroupolis, Greece, July 3–7, 2006; 587–588.
8. Iliopoulos AP. Digital image processing on experimental mechanics and applications on metallic sheets. *Ph.D. Thesis*, National Technical University of Athens, Heroon Polytechniou 9, 15780 Zografou, Greece, 2007.
9. Iliopoulos AP, Andrianopoulos NP. An approach to analyse errors introduced in the random grid strain measurement method. *Strain* 2008; **46**(3):258–266. DOI: 10.1111/j.1475-1305.2008.00444.x. http://onlinelibrary.wiley.com/doi/10.1111/j.1475-1305.2008.00444.x/abstract.
10. Iliopoulos AP, Michopoulos JG, Andrianopoulos NP. Performance sensitivity analysis of the Mesh-Free Random Grid method for whole field strain measurements. *ASME Conference Proceedings* 2008; **2008**(43277):545–555. DOI: 10.1115/DETC2008-49732. http://link.aip.org/link/abstract/ASMECP/v2008/i43277/p545/s1.
11. Iliopoulos AP, Michopoulos JG. Effects of anisotropy on the performance sensitivity of the Mesh-Free random grid method for whole field strain measurement. *ASME Conference Proceedings* 2009; **2009**(48999):65–74. DOI: 10.1115/DETC2009-86962. http://link.aip.org/link/abstract/ASMECP/v2009/i48999/p65/s1.
12. Michopoulos JG, Iliopoulos AP. A computational workbench for remote full field 2D displacement and strain measurements. *ASME Conference Proceedings* 2009; **2009**(48999):55–63. DOI: 10.1115/DETC2009-86900. http://link.aip.org/link/abstract/ASMECP/v2009/i48999/p55/s1.
13. Iliopoulos AP, Michopoulos JG, Andrianopoulos NP. Performance Analysis of the Mesh-Free Random Grid Method for Full-Field Synthetic Strain Measurements. *Strain* 2010; **48**(1):1475–1305. DOI: 10.1111/j.1475-1305.2010.00786.x. http://dx.doi.org/10.1111/j.1475-1305.2010.00786.X.
14. Michopoulos J, Iliopoulos A. A computational workbench for remote full field 3D displacement and strain measurements. *Proceedings of the ASME 2011 International Design Engineering Technical Conferences & Computers and Information in Engineering Conference IDETC/CIE*, Washington, DC, USA, August 29-31, 2011; 489–498.

15. Iliopoulos A, Michopoulos J, Orifici AC, Thomson RS. Experimental validation of the 2D meshless random grid method. *Proceedings of the ASME 2011 International Design Engineering Technical Conferences & Computers and Information in Engineering Conference IDETC/CIE*, Washington, DC, USA, August 29-31, 2011; 512–520.
16. Templeton DW. Computerization of carrier fringe data acquisition, reduction, and display. *Experimental Techniques* 1987; **11**(11):26–30. DOI: 10.1111/j.1747-1567.1987.tb00636.x. http://dx.doi.org/10.1111/j.1747-1567.1987.tb00636.X.
17. Bulhak J, Surrel Y. Grating shearography. *Proceedings of the SPIE, Interferometry '99: Techniques and Technologies*, Vol. 3744, Malgorzata Kujawinska; Mitsuo Takeda, Pultusk Castle, Poland, October 20, 1999; 506–515.
18. Rastogi PK. Speckle shearing photography: a tool for direct measurement of surface strains. *Applied Optics* 1998; **37**(8):1292–1298. DOI: 10.1364/AO.37.001292. http://ao.osa.org/abstract.cfm?URI=ao-37-8-1292.
19. Wasowski JJ, Wasowski LM. Computer-based optical differentiation of fringe patterns. *Experimental Techniques* 1987; **11**(3):16–18. DOI: 10.1111/j.1747-1567.1987.tb00654.x. http://dx.doi.org/10.1111/j.1747-1567.1987.tb00654.X.
20. Post D, Han B. *Springer Handbook of Experimental Solid Mechanics* (Sharpe WN, Jr., ed.) Springer: New York, USA, 2008. Part C. Chapter 22.
21. Mast P, Beaubien L, Clifford M, Mulville D, Sutton S, Thomas R, Tirosh J, Wolock I. A semi-automated in-plane loader for materials testing. *Experimental Mechanics* 1983; **23**:236–241. DOI: 10.1007/BF02320415. http://dx.doi.org/10.1007/BF02320415.
22. Mast PW, Nash GE, Michopoulos JG, Thomas RW, Badaliance R, Wolock I. Experimental determination of dissipated energy density as a measure of strain-induced damage in composites. *Tec. Rpt. NRL/FR/6383–92-9369*, Naval Research Laboratory, Washington, DC, USA, 1992.
23. Mast P, Nash G, Michopoulos J, Thomas R, Wolock I, Badaliance R. Characterization of strain-induced damage in composites based on the dissipated energy density part I. Basic scheme and formulation. *Theoretical and Applied Fracture Mechanics* 1995; **22**(2):71–96. http://www.scopus.com/inward/record.url?eid=2-s2.0-0029274706&partnerID=40&md5=87cbf6af5c303a366dc872fb7c55ad9c.
24. Michopoulos J. *Recent Advances in Composite Materials: In Honor of S.A. Paipetis* (Gdoutos EE, Marioli-riga Z, eds), chap. Computational and Mechatronic Automation of Multiphysics Research for Structural and Material Systems. Kluwer Academic Press: Dordrecht, The Netherlands, 2003, 9–21.
25. Michopoulos J. Mechatronically automated characterization of material constitutive respone. In *Proceedings of the 6th World Congress on Computational Mechanics (WCCM-VI)*. Tsinghua University Press and Springer: Beijing China, September 5–10, 2004; 486–491.
26. Michopoulos J, Hermanson J, Furukawa T. Towards the robotic characterization of the constitutive response of composite materials. *Composite Structures* 2008; **86**(1-3):154–164. DOI:10.1016/j.compstruct.2008.03.009. http://www.scopus.com/inward/record.url?eid=2-s2.0-46949097860&partnerID=40&md5=25dddce389c9640db7cf8fbf3c50dc4e.
27. Cheng P, Sutton M, Schreier H, McNeill S. Full-field speckle pattern image correlation with B-spline deformation function. *Experimental Mechanics* 2002; **42**:344–352. DOI: 10.1007/BF02410992. http://dx.doi.org/10.1007/BF02410992.
28. Hartley R, Zisserman A. *Multiple View Geometry in Computer Vision*, 2nd ed. Cambridge University Press: Cambridge, UK, 2004.
29. Mase G. *Schaum's Outline of Continuum Mechanics*, 1st ed. McGraw-Hill: New York, USA, 1969.
30. Belytschko T, Krongauz Y, Organ D, Fleming M. Meshless methods: an overview and recent developments. *Computer Methods In Applied Mechanics And Engineering* 1996; **139**:3–47. http://citeseerx.ist.psu.edu/viewdoc/summary?doi=10.1.1.132.8046.
31. Lu YY, Belytschko T, Gu L. A new implementation of the element free galerkin method. *Computer Methods in Applied Mechanics and Engineering* 1994; **113**(3-4):397–414. http://www.scopus.com/inward/record.url?eid=2-s2.0-0028400170&partnerID=40&md5=99f50ad6a405b5b4ea436fd3d3a2b77a, cited By (since 1996) 379.
32. Liu GR. *Mesh Free Methods: Moving Beyond the Finite Element Method*, 1st ed. CRC Press: Boca Raton, USA, 2002.
33. Wang J, Liu G. On the optimal shape parameters of radial basis functions used for 2-d meshless methods. *Computer Methods in Applied Mechanics and Engineering* 2002; **191**(23–24):2611 –2630. DOI: 10.1016/S0045-7825(01)00419-4. http://www.sciencedirect.com/science/article/pii/S0045782501004194.
34. Lekhnitskii SG. *Theory of Elasticity of an Anisotropic Elastic Body*. Mir Publishers: Moscow, 1981.
35. Savin GN. *Stress Concentration Around Holes*. Pergamon Press: London, 1961.
36. Chern S, Tuttle M. On displacement fields in orthotropic laminates containing an elliptical hole. *Journal of Applied Mechanics* 2007; **67**:527–539.